Fluid Dynamics &
Materials Processing

Tech Science Press

http://doi.org/10.32604/fdmp.2026.075131

ARTICLE

Injection Damage in Tight Oil Reservoirs: Coupled Scaling and Fouling Mechanisms

**Yong Wang[1,2], Qingqing Cao[3], Changhao Yan[2], Xinyu Tang[2,3], Dingxue Zhang[1,*]
and Jingyi Zhu[3,*]**

[1]Petroleum Engineering College, Yangtze University, Jingzhou, China
[2]Oil and Gas Technology Research Institute, PetroChina Changqing Oilfield Company, Xi'an, China
[3]National Key Laboratory of Oil and Gas Reservoirs Geology and Exploitation, Southwest Petroleum University, Chengdu, China
[*]Corresponding Authors: Dingxue Zhang. Email: zdx7773@163.com; Jingyi Zhu. Email: zhujingyizoe@163.com

Received: 25 October 2025; Accepted: 19 March 2026; Published: 30 June 2026

ABSTRACT: Injection damage in the M tight oil reservoir is controlled by the coupled effects of inorganic scaling and organic fouling at the pore scale. To clarify the governing mechanisms, this study combines long-duration core flooding, water-chemistry compatibility analysis, and thermodynamic scale prediction with NMR T_2 spectroscopy, mercury intrusion capillary pressure, SEM-EDS characterization, and factor-controlled microfluidic visualization that reproduces reservoir pore geometry and wettability. Core flooding tests reveal permeability reductions of 61 to 73 percent after 12 to 24 hours of injection, indicating progressive contraction of effective flow channels. NMR T_2 spectra demonstrate strong pore-size selectivity: small pores largely retain their porosity, 99.43 and 89.48 percent, whereas medium and large pores experience substantial losses. SEM imaging and elemental mapping show Ca and Ba co-located with carbon within pore spaces, consistent with $CaCO_3$ and $BaSO_4$ precipitation induced by mixing sulfate-rich injection water with formation brine. Microfluidic experiments further decouple the roles of oil presence, hydrocarbon type, wettability, and asphaltene content. In the presence of oil, injection pressure increases from 20.4 to 93.6 kPa, compared with 1.3 to 13.4 kPa without oil, while pore-space retention decreases to 73 percent versus 92 percent. Inorganic scale alone causes only moderate injectivity impairment, whereas oil-mediated deposition raises total pore blockage to approximately 27 percent, accounting for nearly two-thirds of the overall injectivity decline. Heavier n-tetradecane generates larger aggregates and higher pressures than n-hexane. Oil-wet surfaces promote more continuous deposits, faster pressure escalation, and greater loss of open flow area than hydrophilic substrates. Increasing the asphaltene surrogate concentration from 2 to 6 percent accelerates inlet bank formation and early throat occlusion, reducing pore-space retention from 98.0 to 67.9 percent and increasing pressure from 59.09 to 78.23 kPa.

KEYWORDS: Tight oil reservoir; microfluidic visualization; formation damage; permeability reduction; asphaltene deposition; carbonate and sulfate scaling

1 Introduction

The development of tight oil reservoirs has become increasingly important given their abundant reserves and potential for future production [1]. Waterflooding is typically essential to exploit such tight oil reservoirs, including the Longdong area of the Ordos Basin, China. However, maintaining injectivity is challenging: injection wells often exhibit rising pressures and declining intake, with frequent under-injection events due to severe formation plugging [2]. This problem threatens the efficient recovery of tight oil reservoirs, making it critical to understand and mitigate the underlying reservoir damage mechanisms that occur during water injection.

Waterflood-induced formation damage is a multifaceted issue. Incompatible injected and formation brines can mix and precipitate inorganic scales that plug pore throats and reduce permeability [3,4]. Fine particles and clay minerals may be dislodged by injection fluids and migrate, accumulating in pore constrictions—especially in low-permeability sandstones with narrow throats—thereby further impeding flow [5]. Organic factors can compound these problems. The injection process and cooling of reservoir fluids often destabilize heavy oil fractions such as resins and asphaltenes, causing them to precipitate and deposit in pores. These deposits not only block flow paths but also alter rock wettability toward oil-wet, exacerbating injectivity loss [6,7]. Laboratory studies have shown that asphaltene deposition can significantly impair core permeability even under continuous flooding conditions [8]. In addition, oil-water emulsification during injection can generate persistent emulsion droplets or sludge that plug pore channels, sometimes in conjunction with fine solids and scale precipitates to form complex composite blockages [9]. Thus, both inorganic scaling and organic fouling contribute to waterflood formation damage, especially in tight reservoirs.

In Chinese low-permeability oilfields, these issues are well documented. For example, in the Changqing Oilfield's Longdong area, sulfate-rich injected water was found to react with barium in formation water, precipitating barium sulfate ($BaSO_4$) scale and leading to progressive injector plugging [10]. Core flooding experiments on tight oil reservoirs have reported severe permeability decline (up to 65%) after extended water injection, attributed to a combination of precipitated scales, mobilized fines, and organic deposits [11–13]. Zhang et al. observed that mixing reinjection water with formation brine in the Baibao oil field caused instantaneous carbonate/sulfate scaling and a rapid increase in injection pressure [14]. Li et al. reported a marked decline in permeability under extended flooding of tight cores, primarily attributable to emulsified oil droplets and fine particles lodging in pore throats [15]. Farajollahi et al. identified asphaltic components in produced plugging deposits, concluding that asphaltene adsorption and deposition on rock grain surfaces was a dominant cause of injector impairment [16]. Previous investigations have identified relevant damage factors, yet the proposed plugging mechanisms rest mainly on indirect indicators such as overall permeability reduction, effluent characterization, and microscopy conducted after flooding. A remaining knowledge gap is the lack of direct pore-scale observation of how these inorganic and organic processes initiate and interact within the porous media under injection conditions.

Advances in experimental techniques now offer opportunities to investigate waterflood damage with greater fidelity. Standard methods include water chemistry analysis and mineralogical characterization to predict scaling tendencies, as well as core-scale flow experiments to measure permeability loss. Imaging tools like scanning electron microscopy with energy-dispersive X-ray spectroscopy (SEM-EDS) are routinely employed to examine the morphology and composition of pore blocking precipitates after core flood tests [17]. Nuclear magnetic resonance (NMR) T_2 spectra measurements can quantify changes in the pore size distribution before and after water injection, helping identify which pore classes are damaged [18]. While these approaches yield valuable information, they cannot directly visualize the dynamic formation of deposits inside an opaque rock during injection. In contrast, microfluidic modeling has emerged as a powerful technique to observe pore-scale fluid–solid interactions in real time under controlled conditions [19]. Microfluidic "lab-on-chip" experiments use transparent micromodels that simulate porous networks, allowing researchers to watch processes like mineral scaling, fines migration, and multiphase displacements as they occur. For instance, Nikoo and Malayeri (2021) used a microchannel device to study calcium scale formation, revealing the impact of flow hydrodynamics and oil–water interfacial forces on scale deposition [20]. Mehdizad et al. (2022) visualized clay swelling and migration in a glass micromodel, directly confirming how pore plugging by clays evolves and impacts permeability [5]. More recent studies have started to design micromodel geometries that better represent actual reservoir pore structures [21–23]. Gong et al. (2023) combined core flooding with a microfluidic visualization of calcium carbonate ($CaCO_3$) precipitation in an ultra-low permeability reservoir, demonstrating the value of real-time observation in identifying scaling patterns [2]. However, most existing microfluidic studies of formation damage have examined either inorganic or organic phenomena in isolation, often using simplified pore networks and neglecting the presence of crude oil components. The coupled effects of oil-phase chemistry and brine incompatibility on pore-scale plugging remain insufficiently understood.

Despite extensive core-flood evidence of injectivity decline, the pore-scale initiation and coupling of inorganic scaling with oil-derived organic fouling during water injection remain insufficiently constrained, largely due to the opacity of real rocks [20–23]. Here we integrate long-duration core flooding using field brines with post-flood NMR T_2 spectra and SEM–EDS, and we further employ a reservoir-analog, high-pressure micromodel to directly visualize deposition and plugging in real time under controlled wettability and oil-chemistry conditions. The objectives are to (i) identify the dominant pore-scale mechanisms responsible for injectivity decline in the M tight oil reservoir and (ii) quantify the relative severity of key controlling factors (oil presence, hydrocarbon type, wettability, and asphaltene content) within a unified microfluidic framework. This multi-scale, factor-controlled approach provides consistent evidence for coupled organic–inorganic co-deposition and offers practical implications for water-compatibility management and targeted mitigation strategies.

The main novelties of this work are threefold: (i) integrating long-duration core flooding with NMR/SEM-EDS and a reservoir-analog high-pressure micromodel to capture consistent multi-scale evidence of coupled scaling–fouling; (ii) enabling direct visualization of organic–inorganic co-deposition using actual field brines and oil under realistic wettability; and (iii) quantifying the relative severity of key controlling factors (oil presence, hydrocarbon type, wettability, and asphaltene content) within a unified, factor-controlled microfluidic framework.

2 Methodology

2.1 Sample Preparation and Experimental Design

The M tight sandstone reservoir is extremely low permeability and 15% average porosity. The reservoir temperature is around 50°C and pressure about 15 MPa, these values were used in our lab scaling tests. Notably, the formation water is highly saline (1.67×10^4 mg/L, pH $\approx$ 8.1) compared to the injection water (4.67×10^3 mg/L, pH $\approx$ 6.6), a large contrast that causes strong scaling tendencies. We used actual field brines from M reservoir for the experiments. The crude oil is moderately viscous (5–50 mPa·s) with a high asphaltene content (15–17 wt%), reflecting the reservoir's oil composition. Core flood tests were conducted at 50°C and slow flow rate (0.02 mL/min) to replicate reservoir injection conditions and minimize rate-sensitivity. Similarly, microfluidic injections were run at 5 μL/min for 11 h under reservoir temperature (50°C). These parameters ensure that our experimental conditions closely represent the field conditions of the M reservoir.

The sample preparation and designed experiments in this study were shown in Fig. 1. Cylindrical sandstone samples with a diameter of 25.44–25.53 mm and a length of 48.84–50.15 mm were drilled from one block from M Tight Oilfield in Northwest China. One cylindrical sandstone sample was cut out 5 mm thin sections on their end faces for contact angle tests and small cubes of 1 to 2 cm^3 in volume for SEM test. Two cylindrical sandstone samples were subjected to mercury injection capillary pressure (MICP) testing. Three cylindrical sandstone samples were used to measure liquid permeability before and after water injection. For two of the samples, NMR T_2 spectra were also acquired before and after injection. The major instruments and key measurement conditions used in this study are shown in Table 1. The basic parameters of cylindrical sandstone samples for liquid permeability test are shown in Table 2. Offcuts produced during the preparation of cylindrical sandstone plugs were collected. They were ground into granules of a specified particle-size range. The ground samples were used for mineral swelling tests and X-ray diffraction (XRD) analysis.

Formation water was sampled on site in the M Tight Oilfield. Water-quality analyses were performed by ion chromatography using an IC761 instrument on formation water, injection water, and treated wastewater. Scaling tendency was predicted at reservoir temperature and pressure using a thermodynamic model. Crude-oil samples were collected from producing wells. Oil viscosity was measured. SARA fractions, including saturates, aromatics, resins, and asphaltenes, were determined.

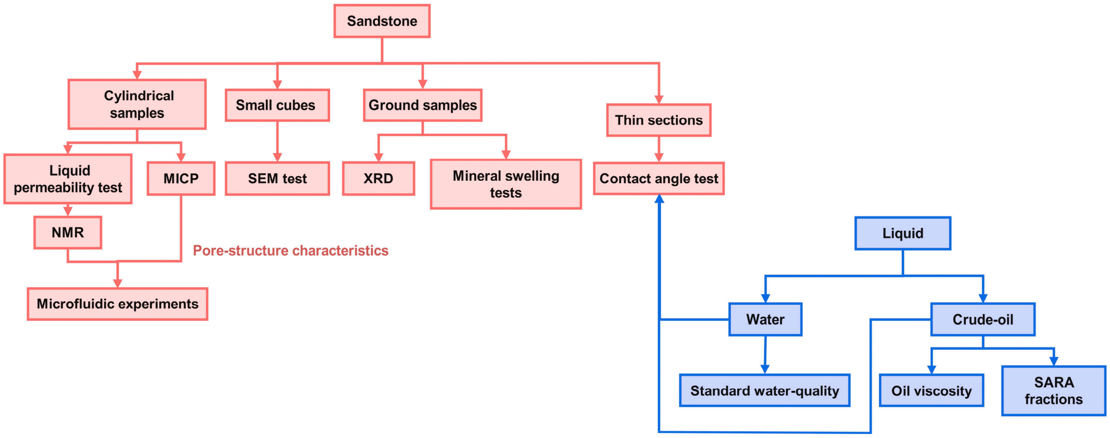

Figure 1: The sample preparation and designed experiments in this study.

Table 1: Instruments used in this study.

Test/Analysis	**Instrument (Model)**
Major ions in brines (formation/injection/treated water)	Ion chromatography system (761 Compact IC)
pH	Benchtop pH meter (SevenCompact S220)
Conductivity/TDS	Benchtop conductivity/TDS meter (SevenCompact S230)
Scaling tendency prediction	Thermodynamic scale-prediction software (OLI ScaleChem/OLI Studio)
Crude-oil viscosity	Rotational viscometer (DV2T Touch Screen Viscometer)
SARA fractions	Standard SARA fractionation (ASTM D6560 + modified ASTM D2007)
XRD	X-ray diffractometer (Bruker D8 ADVANCE)
Thin section petrography/point counting	Polarizing microscope (Olympus BX53MTRF-S)
MICP	Mercury intrusion porosimeter (AutoPore IV 9500)
NMR T_2	Low-field core NMR analyzer (MicroMR02-025V, 2 MHz)
SEM imaging and elemental analysis Wettability	ZEISS EVO MA15 + EDS Contact angle goniometer (SDC-200S)

Table 2: The basic parameters of cylindrical sandstone samples for liquid permeability test.

Sample No.	Diameter (mm)	Length (mm)	Permeability (mD)	Porosity (%)
M-1	25.53	48.84	0.071	15.73
M-2	25.44	50.03	0.097	13.86
M-3	25.46	50.15	0.394	14.97

2.2 Fluid and Rock Characterization

2.2.1 Brine Ionic Composition and Salinity

Formation water, injection water, and treated wastewater were collected on site and filtered prior to analysis. Major cations (K^+, Na^+, Ca^{2+}, Mg^{2+}, Ba^{2+}, Sr^{2+}) and anions (Cl^-, $SO_4{}^{2-}$, $CO_3{}^{2-}$, Br^-) were quantified by ion chromatography (IC; instrument: IC761) following routine calibration with multi-ion standards. Total dissolved solids (TDS) and pH were measured to support compatibility evaluation.

2.2.2 Thermodynamic Scaling Tendency Prediction

The measured ion compositions, pH, and fluid density were used as inputs to a thermodynamic scale-prediction workflow at reservoir conditions (50°C, 15 MPa). Electroneutrality was enforced and mixed-water cases were simulated to obtain scale indices and equilibrium precipitate amounts for carbonate and sulfate minerals.

2.2.3 Crude-Oil Viscosity and SARA Fractions

Crude oil was sampled from producing wells. Viscosity was measured at the test temperature using a rotational viscometer. SARA fractions were determined using standard fractionation procedures to quantify heavy-component content relevant to organic fouling.

2.2.4 Mineralogy, Pore Structure, and Wettability

Whole-rock and clay-mineral compositions were determined by X-ray diffraction (XRD), and thin-section petrography with point counting was conducted to identify lithofacies and cementation features. Pore-structure characteristics were obtained from mercury intrusion capillary pressure (MICP) and NMR T_2 measurements. Wettability was evaluated by contact-angle measurements on polished end-face thin sections using a contact-angle goniometer.

2.3 Liquid Permeability Test

An unconventional formation-damage evaluation apparatus was used to measure core permeability before and after long-duration water injection. The measurement followed Darcy's law [24]. The core was first saturated with formation water and flowed until a stable pressure drop was obtained. Injection water was then introduced at a constant flow rate equal to the formation-water rate. Between 5 and 500 pore volumes were injected to allow full interaction between the two waters. After displacement, the post-injection permeability was measured under the same temperature (50°C).

2.4 Microfluidic Experiments

Pore-structure characteristics were obtained from NMR and MICP. Microfluidic chips with irregular geometries were designed. Their sizes were 6 mm × 4 mm × 3 μm. Channels were laser-etched on glass according to the design patterns. The chips replicate the pore structure of the reservoir cores. They were used for microfluidic experiments. The pore network was etched in PDMS. The channel depth was 3 μm. The chip withstood 5 MPa under rigid support and permanent bonding. The inlet orifice had a 1.4 mm diameter to ensure compatibility with the injection system. The two chips had an average pore radius of 45.44–46.53 μm, which matched the target reservoir [25]. A custom-fabricated microfluidic chip was made by laser-etching an irregular pore network into PDMS (polydimethylsiloxane), which was then bonded to a glass slide for support. This design recreates the M reservoir's pore geometry while allowing high-pressure operation (rated up to 5 MPa) and optical transparency for visualization.

In this study, we systematically vary wettability, oil type (saturated hydrocarbon chain length), and asphaltene content in the microfluidic experiments, because these factors reflect key field conditions of the M reservoir. The reservoir rock is known to be oil-wet, so comparing hydrophilic vs. hydrophobic conditions reveals wettability effects on scaling. The oil composition is varied to represent different hydrocarbon fractions—higher molecular-weight, more viscous oils are expected to aggravate scaling by increasing flow resistance and precipitation tendency, similar to the heavier components present in the M reservoir crude. Asphaltene content is specifically examined since the M reservoir's crude oil contains an unusually high asphaltene fraction; asphaltenes can precipitate during water injection and cause severe pore plugging, especially when coupled with inorganic scale. By selecting these factors, our microfluidic tests directly address the conditions thought to cause formation damage in the field.

Photograph of the microfluidic experimental platform is shown in Fig. 2. An image acquisition system recorded video and captured images throughout the experiment. A pressure monitoring system collected pressure data over the entire run. Injection pressure as a function of injected volume was obtained by calculation and analysis. Fluids were injected at 5 μL per minute for 11 h. The temperature was maintained at 50°C, equal to the reservoir temperature.

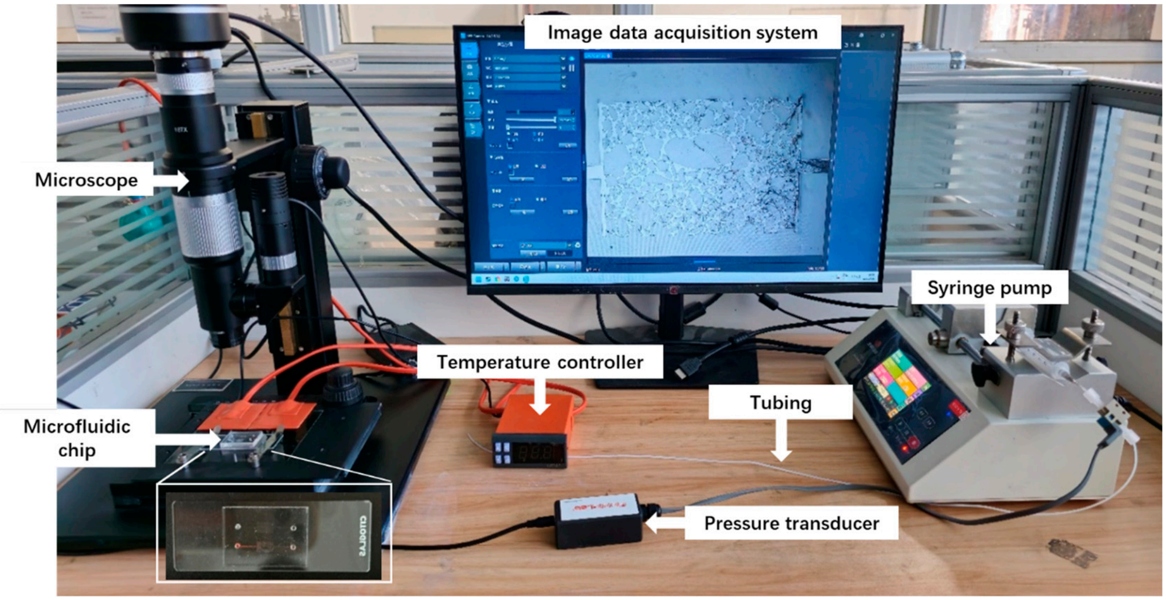

Figure 2: Photograph of the microfluidic experimental platform.

The water-injection experiment on the microfluidic platform was conducted as follows.

(1) Injection water pre-stained with a red dye was loaded into a syringe and mounted on a syringe pump.

(2) The video microscope was focused and the motorized stage was adjusted until the chip was centered and sharply imaged on the display.
(3) The resistive heater was switched on and the temperature was set to the target reservoir value.
(4) A gradient injection protocol was programmed on the pump to deliver the liquid at controlled flow rates, ensuring that the pore network within the chip was fully saturated.
(5) The microscope video software was started to record the entire injection process, and the pressure-monitoring software was run in parallel to continuously log the injection pressure.

To elucidate how the oil–water system, reservoir wettability, and asphaltenes influence complex scale formation, a series of multi-factor microfluidic chip experiments was designed with controlled variations in these factors. The experimental procedure and grouping scheme are summarized in Table 3. It should be noted that VO-79 (anthrone violet) was selected as a macromolecular surrogate for crude-oil asphaltenes. VO-79 is a heavy polyaromatic compound (molecular weight ~712) with bulky ring structures and alkyl side chains, was selected because its chemical nature (high hydrophobicity and tendency to aggregate) closely mimics crude oil asphaltenes.

Table 3: Design of experiments and number of groups for each factor.

Chip No.	Wettability	Oil Type/Condition	VO-79 (wt%)	Injection Sequence
1	hydrophilic glass (water-wet)	no oil	0	formation water → injection water
2	hydrophobic/oil-wet analogue	kerosene	0	kerosene → formation water → injection water
3	(as designed)	n-hexane	0	n-hexane saturation → formation water → injection water
4	(as designed)	n-tetradecane	0	n-tetradecane saturation → formation water → injection water
5	hydrophilic glass	(no extra oil)	0	formation water → injection water
6	hydrophobic PDMS	(no extra oil)	0	formation water → injection water
7	(as designed)	oil + VO-79	2	oil (2% VO-79) → formation water → injection water
8	(as designed)	oil + VO-79	6	oil (6% VO-79) → formation water → injection water

In this study, a long-duration end-point protocol was adopted to quantify macroscopic permeability damage. Therefore, permeability was measured before injection and after the designed long-term injection window (5–500 PV) rather than continuously recorded as a function of injected volume.

3 Results and Discussion

To align with the experimental workflow in Section 2, the Results and Discussion are presented in the following order: (1) fluid and rock characterization, (2) core-scale permeability damage evaluation, and (3) factor-controlled microfluidic visualization.

3.1 Liquid Properties

3.1.1 Formation Water, Injection Water, and Treated Wastewater

Samples of formation water, injection water, and treated wastewater from the M Tight Oilfield were analyzed for ionic composition and salinity, as summarized in Table 4. The formation water exhibited high salinity (TDS 16,683.5 mg/L) with pH 8.15. The injection water had TDS 4672.1 mg/L and pH 6.65, whereas the treated wastewater showed TDS 7692.4 mg/L and pH 7.80. Mixing the formation water with either re-injection water or treated wastewater involves pronounced salinity contrasts and pH differences, indicating poor compatibility and a heightened risk of mineral scaling; accordingly, scaling propensity and mixing-compatibility tests were performed [25,26].

Table 4: Ionic composition and salinity of formation water, injection water, and treated wastewater from the M Tight Oilfield.

Water Sample Type	**Salinity (mg/L)**	**Positive Ion (mg/L)**						**Negative Ion (mg/L)**			
		K^+	**Na^+**	**Ca^{2+}**	**Mg^{2+}**	**Ba^{2+}**	**Sr^{2+}**	**CO_3^{2-}**	**SO_4^{2-}**	**Br^-**	**Cl^-**
Formation water	16,683.5	32.9	6046.8	518.3	131.8	15.7	54.0	150.6	197.1	9.4	9526.9
Injection water	4672.1	15.5	1323.1	272.5	164.9	0	4.9	28.4	1977.1	9.2	876.5
Treated wastewater	7692.4	109.1	2665.8	405.7	58.0	0.5	6.2	105.6	572.9	2.9	3765.7

In accordance with Sulin's water-type classification, the equivalent ratio of residual Cl^- to Mg^{2+} in the formation water exceeds unity, indicating a $CaCl_2$-type water. Applying the same procedure to the injection water and the treated wastewater yields Na_2SO_4-type and $CaCl_2$-type waters, respectively.

3.1.2 Ionic Scaling Tendency Prediction

Scaling cations of the formation water are present at appreciable levels, with Ca^{2+} is 518.3 mg/L and Ba^{2+} is 15.7 mg/L. The anion composition shows SO_4^{2-} is 197.1 mg/L and CO_3^{2-} is 150.6 mg/L. Under alkaline conditions, the carbonate concentration implies a clear tendency for $CaCO_3$ precipitation through Ca^{2+}–CO_3^{2-} combination. Although Ba^{2+} is relatively low, the coexistence of sulfate indicates a non-negligible risk of $BaSO_4$ scale. The injected water contained 1977.1 mg/L of SO_4^{2-}. When such a sulfate-rich stream mixes with formation water in which sulfate is relatively scarce, the chemical environment favors precipitation with resident Ba^{2+} and Sr^{2+}, forming $BaSO_4$ and $SrSO_4$. In addition, the treated wastewater carried 405.7 mg/L of Ca^{2+}, a level comparable to the Ca^{2+} in the formation water. After mixing in the reservoir, carbonate scaling is therefore expected through reaction of Ca^{2+} with dissolved CO_3^{2-}, producing $CaCO_3$ deposits. These results indicate a pronounced risk of sulfate and carbonate scale formation during injection.

A thermodynamic scale-tendency model was used to evaluate formation water, injection water, and treated wastewater under reservoir conditions (50°C and 15 MPa). Ion species and concentrations, density, and pH were specified, electroneutrality was enforced and blends were reconciled, and simulations were run at 50°C and 15 MPa. The software returned phase-specific scale indices and equilibrium precipitated concentrations. Results of ionic scaling tendency prediction are shown in Fig. 3. The formation water shows a clear scaling tendency with $CaCO_3$ and $BaSO_4$ precipitation of 82.72 mg/L and 25.75 mg/L, respectively. For the injection water, the predicted precipitates are negligible, with $CaCO_3$, $SrSO_4$, and $SrCO_3$ each less than 1 mg/L, indicating no practical scaling risk. The treated wastewater displays a $CaCO_3$ tendency with a predicted precipitate concentration of 45.55 mg/L. Mixing of either injection water with the formation water *in situ* is therefore expected to promote $CaCO_3$ and $BaSO_4$ scaling in the study area.

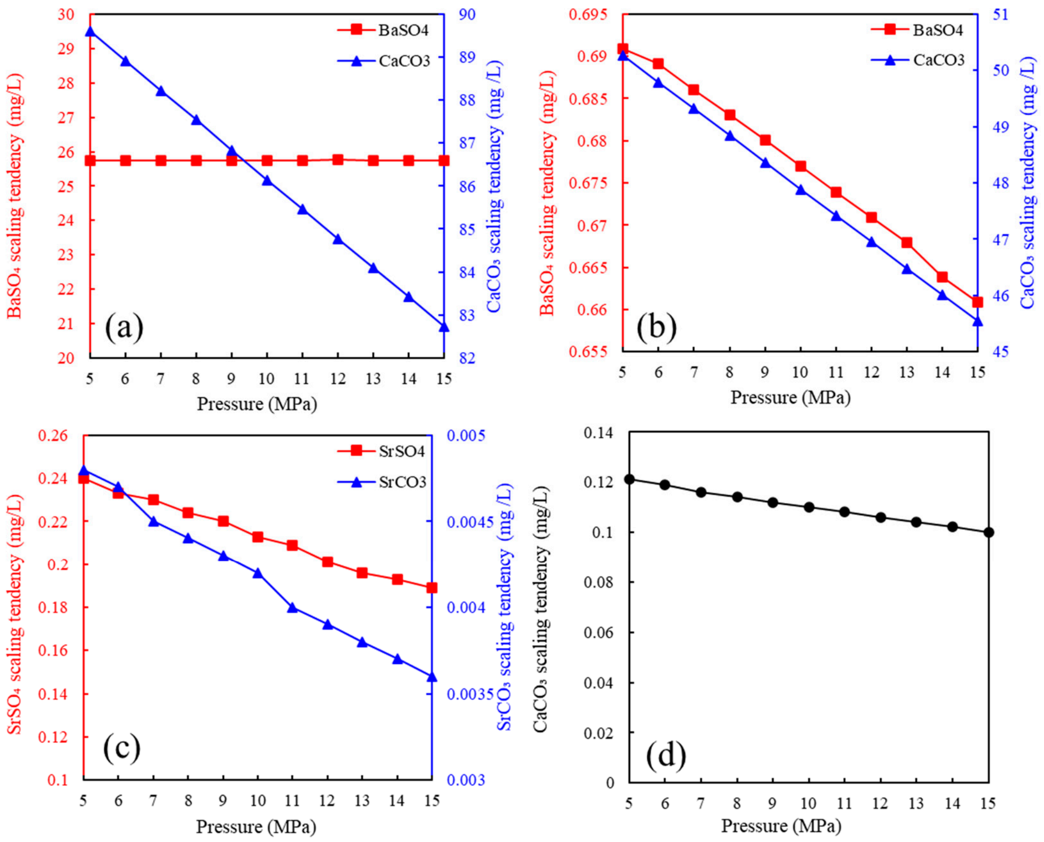

Figure 3: Results of ionic scaling tendency prediction. (**a**) Scaling tendency prediction for formation water. (**b**) Scaling tendency prediction for treated wastewater. (**c**) Scaling tendency prediction of $SrSO_4$ and $SrCO_3$ in injection water. (**d**) Scaling tendency prediction of $CaCO_3$ in injection water.

3.1.3 Crude-Oil

The crude-oil viscosity and SARA analysis are reported in Table 5. The viscosity of the crude-oil ranges from 5 to 50 mPa·s under the test conditions, which, according to the Chinese petroleum and natural gas industry standard SY/T 6169-2021, corresponds to medium-to-high-viscosity crude [27]. A survey of other blocks in the M Tight Oilfield shows asphaltene contents of 1.66%–5.04% [28–30]. By contrast, the asphaltene level in the study area is approximately 3.08–10.16 times higher, implying a strong tendency for pore-throat deposition, deterioration of reservoir connectivity, and adverse impacts on well productivity.

Table 5: Crude-oil viscosity and composition from the M Tight Oilfield.

Sample No.	Viscosity (mPa·s)	Contents (%)			
		Asphaltenes	Saturated Hydrocarbons	Aromatic Hydrocarbons	Non-Hydrocarbons
C-1	25	15.51	64.61	16.63	3.25
C-2	10	16.86	62.86	17.08	3.20

3.2 Petrological Properties

3.2.1 Reservoir Lithology

Whole-rock analysis analyses for three samples from M Tight Oilfield are shown in Fig. 4. Quartz contents are 22.3%~46.6%, with average of 36.7%. Thin-section identification and point counting indicate that the dominant lithofacies in the study area is feldspathic sandstone [25]. Minor clay occurs within quartz grains, and the feldspar population is plagioclase-rich with low to moderate alteration. Calcite is locally present. Lithic fragments are mainly quartzite, microcrystalline rocks, phyllite, and dolomite, whereas the clayey matrix is scarce. Cementation is characterized by chlorite pore-lining films and mosaic calcite, with the chlorite rims contributing to pore preservation. Pyrite and authigenic chlorite are observed sporadically. This framework–cementation architecture suggests a heightened susceptibility to fines migration and scale attachment under water-injection conditions.

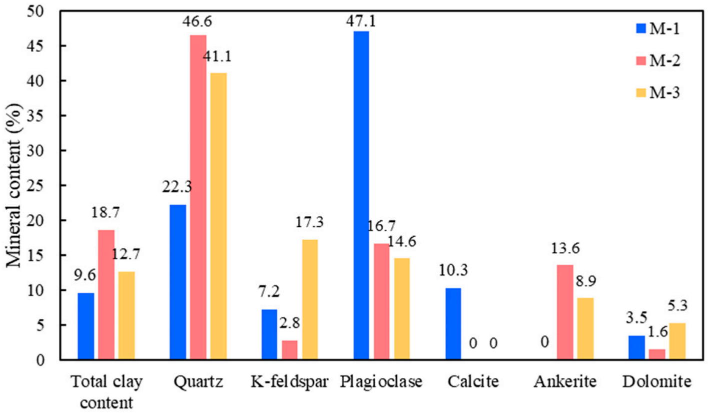

Figure 4: Whole-rock analyses of M Tight Oilfield.

Clay-mineral composition of the M Tight Oilfield indicated the presence of illite, kaolinite, chlorite, and illite-smectite interlayers (Fig. 5). Kaolinite and chlorite were dominant, with kaolinite reaching 67.6% and chlorite up to 38.1% in individual samples. Given the high proportions of kaolinite and chlorite, the M Tight Oilfield is considered highly susceptible to rate sensitivity and acid sensitivity, consistent with an increased tendency for fines migration under flow acceleration and adverse reactions during acidizing. This explains why is used to rule out the possibility of clay swelling being the dominant mechanism.

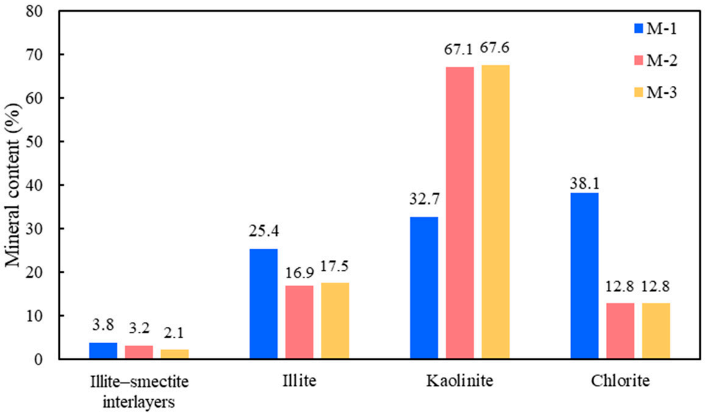

Figure 5: Clay-mineral composition of the M Tight Oilfield.

3.2.2 Pore Structure Characteristics

Fig. 6 shows the pore-radius distribution obtained from MICP for M Tight Oilfield. The pore radii are mainly concentrated in the 5 to 50 μm range, with an average pore radius of 46.48 μm. This provides the scale basis for the microfluidic chip design, echoing the methodology section.

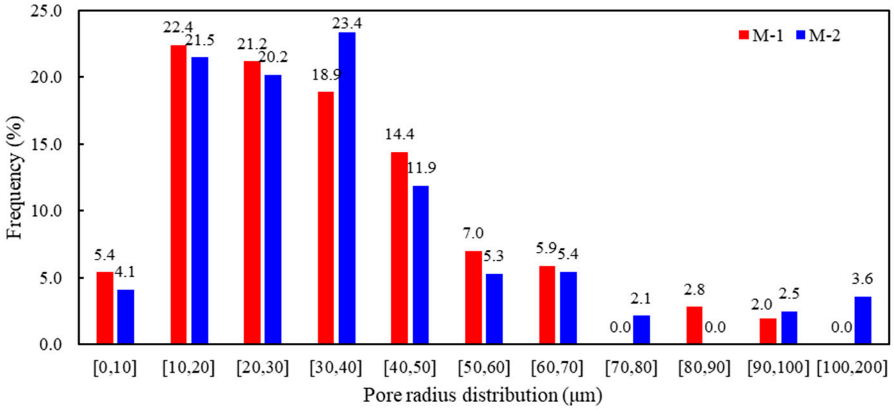

Figure 6: The pore-radius distribution obtained from MICP for the M Tight Oilfield.

SEM images of samples from the M Tight Oilfield are shown in Fig. 7. Large pores and throats offer relatively unobstructed pathways for fluids and suspended particles, whereas small pores exhibit a markedly higher propensity for particle retention and plugging. From a filtration/mechanical entrapment perspective, small pore throats are more prone to capturing fine particles and nascent crystal nuclei due to stronger geometric constriction and bridging effects, as well as their higher specific surface area that promotes adhesion and subsequent scale growth. This size selectivity indicates that mechanical filtration at fine throats is an important contributor to pore-scale plugging.

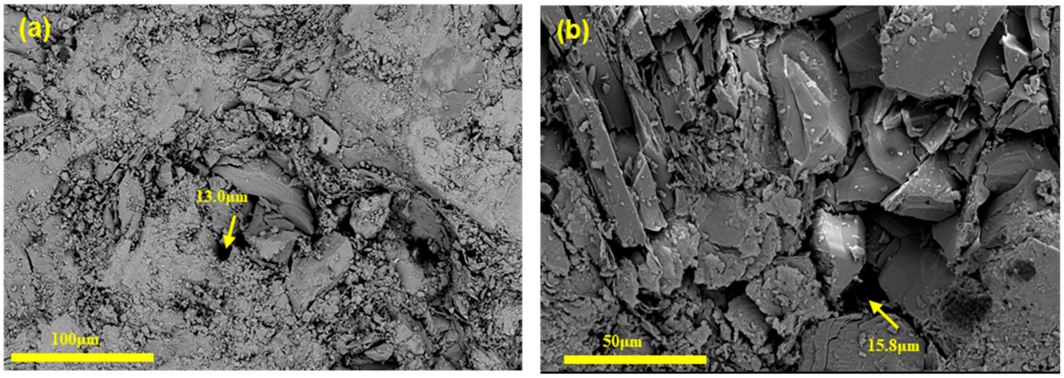

Figure 7: SEM images of samples from the M Tight Oilfield. (**a**) Low-magnification view (scale bar: 100 μm). (**b**) High-magnification view (scale bar: 50 μm).

In line with prevailing practice, pore sizes in tight sandstones are classified by NMR transverse relaxation time (T_2) in small pores ($T_2 \leq 10$ ms), medium pores (10 ms < $T_2 \leq 100$ ms), large pores (100 ms < $T_2 \leq 1000$ ms). Inspection of the T_2 spectra for the two samples shows that the strongest signal peak in both samples falls within 1–10 ms, indicating a predominance of small pores (Fig. 8). This pattern implies that the M Tight Oilfield hosts a well-developed small-pore system, consistent with the tight, ultra-low-permeability nature of the reservoir. The small pores dominate the pore system, making it particularly noteworthy that the subsequent injection-induced damage is mainly concentrated in the medium-to-large pore ranges.

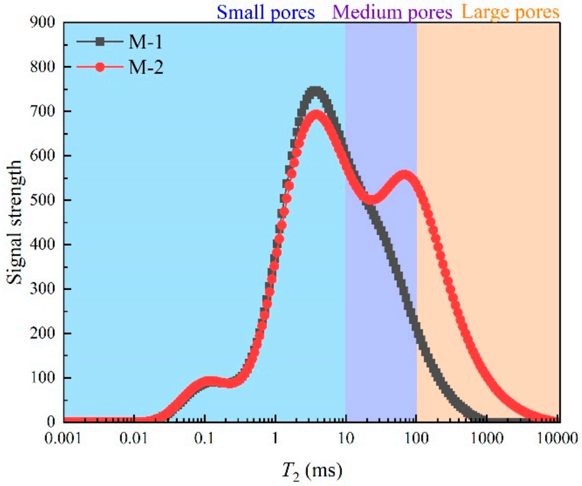

Figure 8: T_2 spectra of samples from the M Tight Oilfield.

3.2.3 Contact Angle Tests

Contact angle tests for the water and oil phases are shown in Fig. 9. The water and oil contact angles of M-1 were 112.4° and 24.2°, respectively. For M-2, the values were 76.6° and 16.6°, and for M-3 they were 68.8° and 17.8°. Taken together, the oil-phase contact angles of samples are uniformly below 75°, and the water-phase angles of samples are high, especially for M-1, indicating an oil-wet to moderately oil-wet surface. In such hydrophobic matrix, injected water exhibits limited spreading on the mineral surface, capillary forces oppose displacement, and the efficiency of water injection is reduced due to poorer sweeping and greater resistance to flow. An oil-wet substrate can promote scale aggregation by restricting water-film spreading and increasing local residence time.

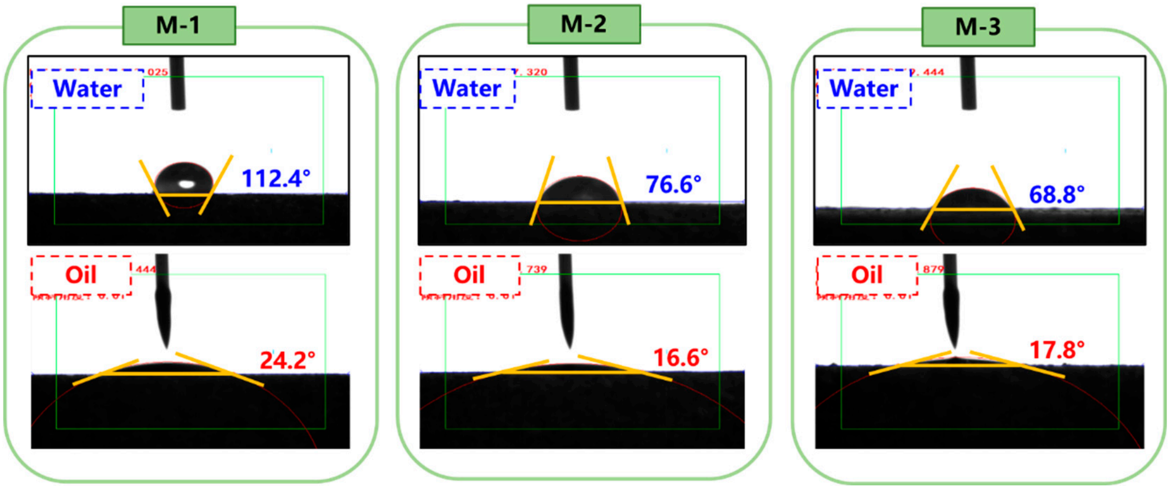

Figure 9: Contact angle test results of samples from the M Tight Oilfield.

3.3 Evaluation of Water Injection Induced Permeability Damage

3.3.1 Liquid Permeability Test

Liquid permeability test results before and after water injection for three cylindrical sandstone samples are summarized in Table 6. M-1 decreased from 0.071 mD to 0.028 mD, indicating 61% permeability reduction. M-2 declined from 0.097 mD to 0.026 mD, indicating 73% permeability reduction. M-3 dropped from 0.394 mD to 0.121 mD, indicating 69% permeability reduction. After 12–24 h of water injection, permeability consistently decreased and the ability of the cylindrical sandstone samples to transmit fluid was reduced, which implies a contraction of the effective flow pathways within the pore system. The rapid 61%–73% permeability loss and the preferential impairment of medium/large pores indicate that tighter control of sulfate-rich injection-water quality and proactive near-wellbore scale/asphaltene management are required to sustain injectivity in the M reservoir.

Table 6: Liquid permeability test results before and after water injection.

Sample No.	Initial Permeability (mD)	Post-Injection Permeability (mD)	Permeability Reduction
M-1	0.071	0.028	61%
M-2	0.097	0.026	73%
M-3	0.394	0.121	69%

One contributor to the permeability decline is fines migration during water injection. The rock matrix is subjected to hydrodynamic scouring, causing detachment and transport of microparticles and clay from cements, which subsequently accumulate in pore throats and impede flow, thereby reducing permeability [31]. A second contributor is mineral scaling arising from incompatibility between injected water and formation water, with the precipitated scales further blocking pore spaces and exacerbating injectivity loss [32].

Although a continuous core-scale permeability–injected-volume curve is not available due to the end-point design, the time-/volume-resolved microfluidic pressure responses and pore-space retention analyses provide dynamic evidence for the evolution of plugging during water injection, which is consistent with the observed 61%–73% permeability reduction in the core tests.

3.3.2 Mineral Swelling Test

Water sensitivity of the reservoir was weak, and pore-throat occlusion caused by clay-mineral swelling was not the dominant cause of permeability loss. As shown in Fig. 10, mineral powders soaked in injected water for 24 h and 48 h did not exhibit appreciable expansion, the solid volume remained at approximately 4 mL, and the swelling ratio was only 2.3%. These observations indicate that the permeability reduction observed after water injection is attributable primarily to scale formation and pore blockage arising from incompatibility between the injected water and the formation water, rather than to clay-swelling effects. The weak swelling response indicates that clay swelling is unlikely to be the dominant mechanism, thereby supporting our interpretation that incompatibility-induced scaling coupled with fines migration governs the observed damage.

3.3.3 Evolution of Pore Structure after Water Injection

From the evolution of the T_2 distributions before and after water injection, as shown in Fig. 11, water injection induced permeability damage to small pores is minimal, whereas the principal scaling response occurs in the medium and large pore domains. The T_2 spectra after water injection 12 h were integrated to quantify pore class changes, and the porosity retention rates were used to characterize pore-scale damage (Fig. 12). For the two samples, the porosity retention rates of small pores reached 99.43% and 89.48%, respectively. With increasing pore size, the degree of damage increased. The porosity retention rates of medium and large pores of M-1 were 86.37% and 62.41%, respectively. The porosity retention rates of medium and large pores of M-2 were 59.43% and 56.35%, respectively.

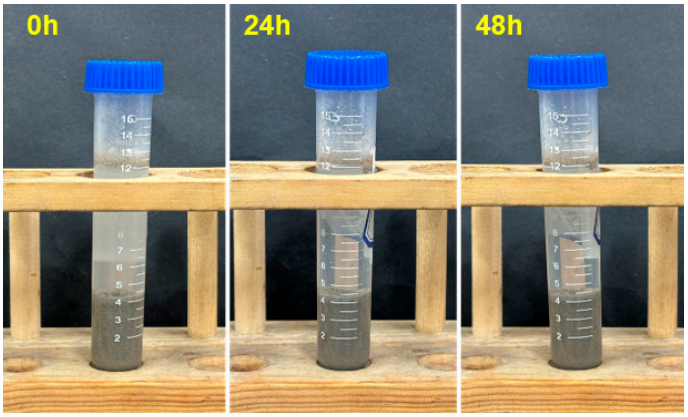

Figure 10: Mineral swelling test results.

During water injection the injected phase partitions preferentially into low-resistance pathways, so pores and throats with larger characteristic radii carry a disproportionate share of the flux. This follows from Darcy-type flow in porous media and the strong radius dependence of hydraulic conductance and permeability predicted by capillary and critical-path models, whereby channels with larger pore-throat sizes impose lower viscous losses and thus attract more throughput [33]. As throughput increases in these conduits, the contact area and contact time between injected and formation waters also increases, enhancing ionic mixing, resulting in promoting carbonate and sulfate scaling in the near-wellbore and formation matrix [34]. These mixing-induced precipitation processes and their prediction by saturation-index/thermodynamic models are well documented for $CaCO_3$, $BaSO_4$ and related scales. Consistent with this flow partitioning, the pronounced 10–100 ms peak observed in sample M-1 on the T_2 spectra indicates an abundance of medium pores with a contribution from large pores, which are more likely to capture the injection water and thus to experience stronger scaling and solid deposition under mixing.

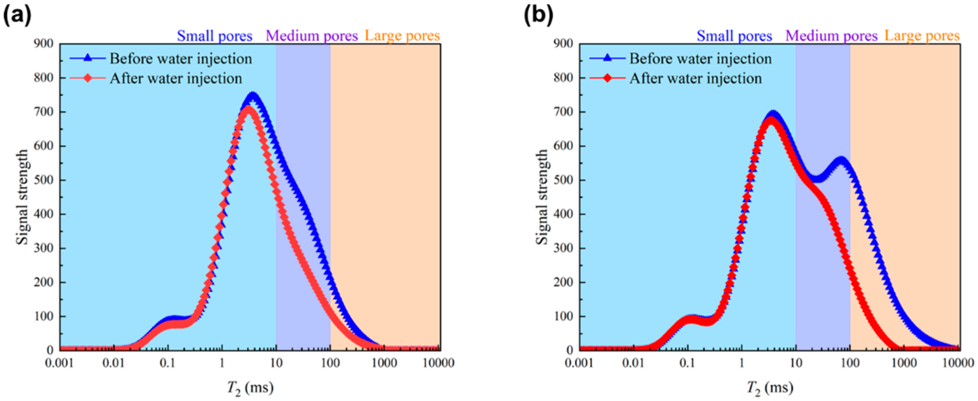

Figure 11: T_2 spectra of samples from the M Tight Oilfield before and after water injection. (**a**) M-1. (**b**) M-2.

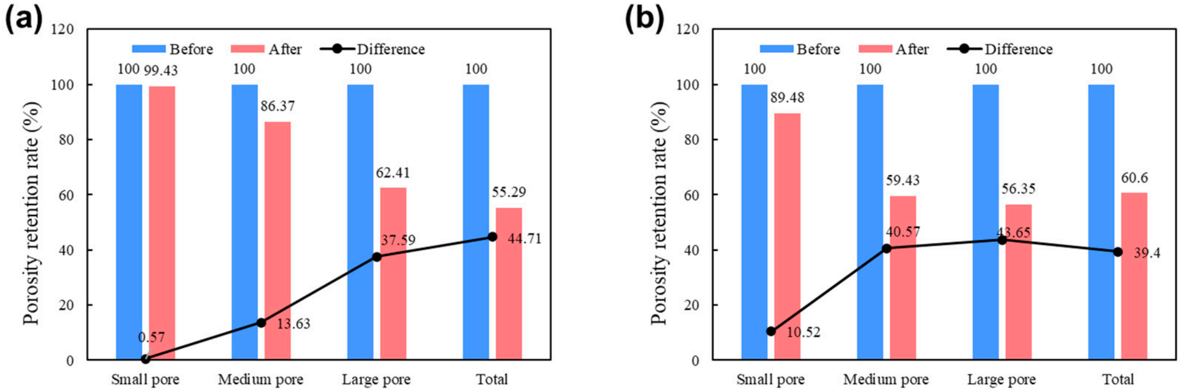

Figure 12: Porosity retention rates of samples from the M Tight Oilfield before and after water injection. (**a**) M-1. (**b**) M-2.

SEM image of the initial sample (Fig. 13a) shows a well-developed pore system with clean and relatively smooth pore walls. The post-injection SEM image (Fig. 13b) shows irregular granular deposits around pores, an increased abundance of extraneous particles, and less distinct pore apertures. In contrast to the initial sample, the post-injection sample exhibits clear Ca and Barium (Ba) signals, indicating the formation of $CaCO_3$ and $BaSO_4$ inorganic scales (Fig. 13c,d). Elemental mapping of the post-injection sample further shows spatial co-location of carbon (C) and calcium (Ca) within pore regions, consistent with $CaCO_3$ infilling of the pore space. Elemental analyses by EDS for the initial and post-injection samples are summarized in Fig. 14 and the quantitative elemental composition by EDS is shown in Table 7. The pre-injection sample is dominated by O, Si and Al peaks with minor C/Mg (and trace Fe), while the Au signals originate from sputter coating. No evident Ca or Ba peaks are observed before injection. After injection, distinct Ca and Ba peaks emerge in addition to the matrix-related O–Si–Al signals, indicating the occurrence of inorganic scale deposition (likely $CaCO_3$ and $BaSO_4$); Au peaks are associated with sputter coating. After injection, the emergence of Ca and Ba signals and their co-localization with pore locations support pore filling by $CaCO_3$ and $BaSO_4$. Taken together, the morphological evidence in Fig. 13 and the quantitative elemental results in Fig. 14 jointly confirm that inorganic scaling indeed occurred.

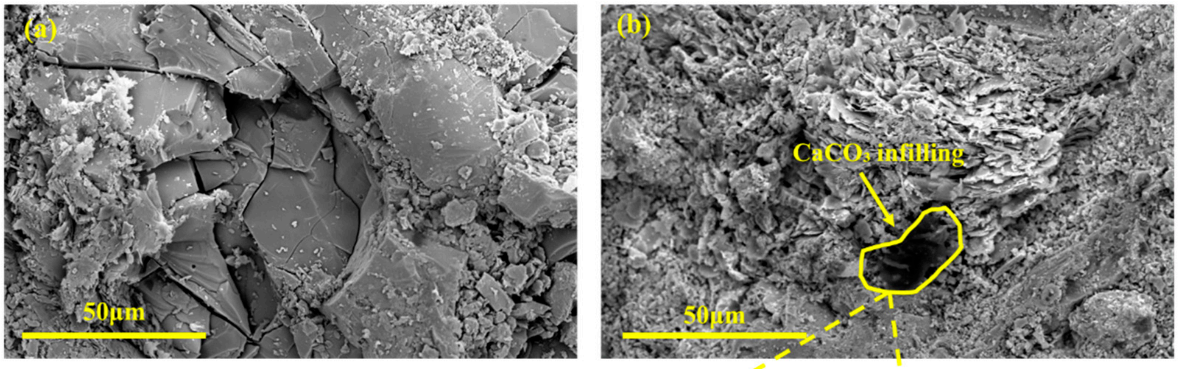

Figure 13: *Cont.*

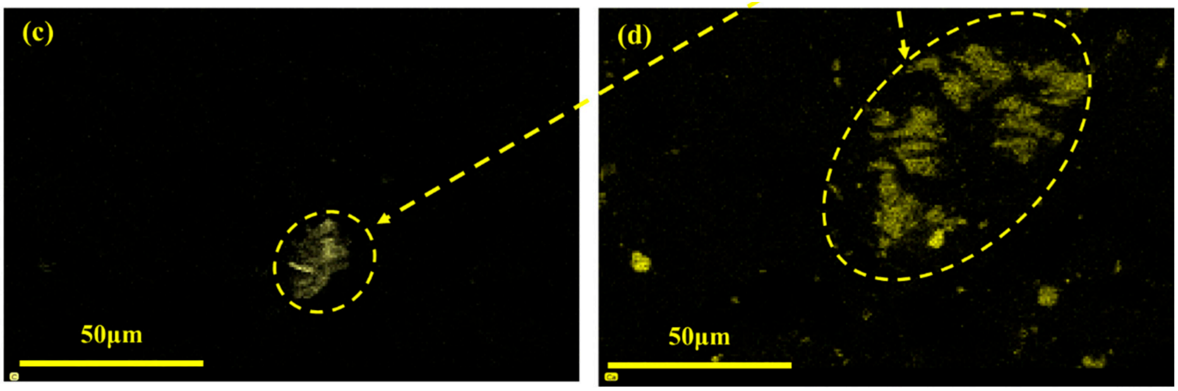

Figure 13: SEM images and elemental maps of initial and post-injection samples from the M Tight Oilfield. (**a**) Initial sample. (**b**) Post-injection sample. (**c**) Carbon elemental map of the post-injection sample. (**d**) Calcium elemental map of the post-injection sample.

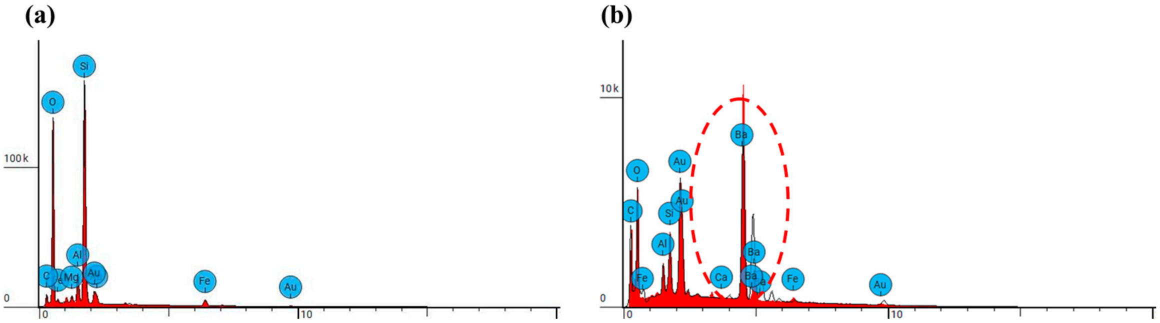

Figure 14: Elemental analyses by EDS for the initial and post-injection samples from the M Tight Oilfield. (**a**) Initial sample. (**b**) Post-injection sample.

Table 7: The quantitative elemental composition by EDS for the initial and post-injection samples from the M Tight Oilfield.

Initial Sample		Post-Injection Sample	
Element Symbol	**Weight Conc. (%)**	**Element Symbol**	**Weight Conc. (%)**
C	2.8	C	16.1
O	38.7	O	33.9
Na	0.9	Mg	0.8
Mg	1.3	Al	10.0
Al	8.5	Si	15.7
Si	23	K	2.5
S	0	Ca	0.8
K	2.1	Fe	7.0
Ca	0.8	Sr	0.8
Fe	5.8	Ba	0.7
Au	16.1	Au	11.6

3.4 Microfluidic Experiments

3.4.1 Effect of Oil Presence on Scaling Behavior

Fig. 15 shows the migration of scale particles and the ensuing plugging of pores and throats during injection in two microfluidic chips designed to isolate oil-water property effects. Dark regions denote scale deposits. In the oil-free chip (Chip 1), deposits initially appear as small dot-like or patchy features adhering to the substrate, then grow progressively as the cumulative volume of injection water increases. Concurrently, the injection water interacts with formation water retained in local pores, generating new particles that gradually concentrate within the chip. In contrast, the oil-bearing chip (Chip 2) exhibits a markedly larger areal coverage of black deposits, with pronounced particle aggregation, predominantly blocky agglomerates, and the development of band-like accumulations that promote partial to near-complete occlusion of pore throats. The oil phase promotes aggregation by narrowing the effective water-flow channels and prolonging the residence time.

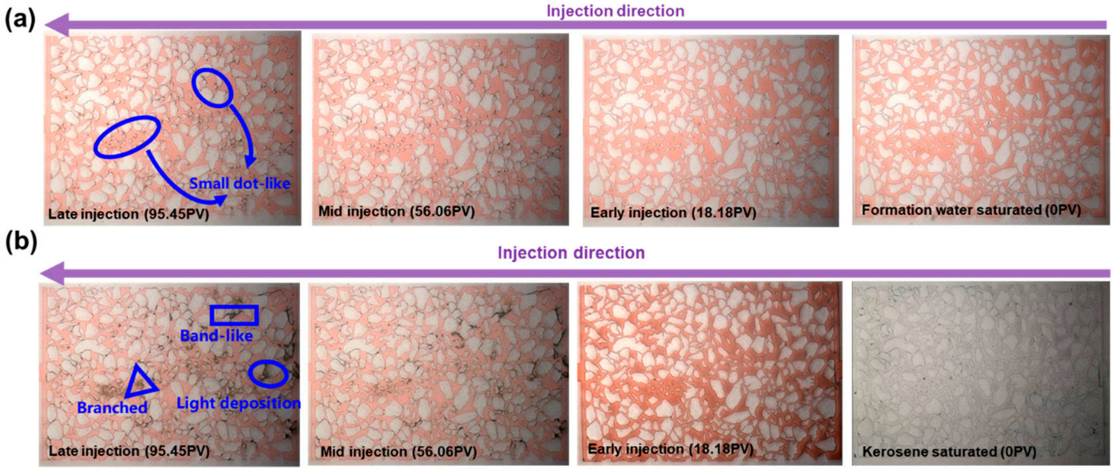

Figure 15: Representative microfluidic images showing scale-deposit evolution during injection of sulfate-rich water into an irregular pore-network micromodel under oil-free versus oil-bearing conditions: (**a**) Chip 1, formation water + injection water; (**b**) Chip 2, kerosene-saturated then formation water + injection water. Dark regions indicate inorganic/organic-associated deposits that progressively occlude pores and throats.

Microscope video recordings show that scaling is substantially more pronounced in Chip 2 than in Chip 1. Quantitative image analysis of Chips 1 and 2 indicates lateral particle sizes of 17–52 μm in Chip 1 and 29–437 μm in Chip 2, confirming accelerated growth and stronger aggregation when oil is present. The oil phase reduces the aqueous flow space, lowers local velocities, and enhances flow non-uniformity, conditions that facilitate particle capture, coalescence, and deposition [35]. Deposited clusters then act as collectors that recruit additional particles, forming larger agglomerates that progressively constrict pore throats and intercept more solids, establishing positive feedback that degrades hydraulic conductivity [36,37].

From the perspective of the saturating oil, kerosene is compositionally analogous to crude oil as a complex mixture of long-chain saturates and aromatics with relatively high viscosity and low aqueous solubility. Upon cooling by injected water, solubility further decreases and organic precipitates form and accumulate within channels, exacerbating blockage. As conduits narrow, residence time increases and mixing between injected and formation waters is intensified, which strengthens scaling reactions and promotes continued deposition.

Injection pressure in Chip 2 was consistently higher than in Chip 1, as shown in Fig. 16. In Chip 1 the pressure increased from 1.3 to 13.4 kPa, whereas in Chip 2 it rose from 20.4 to 93.6 kPa. During the early stage both traces changed gently, but with continued injection the pressures kept rising and the oil-bearing curve became markedly steeper. Linear fits gave slopes of 2.09 for Chip 2 and 0.36 for Chip 1, evidenced by a faster pressure build-up in the presence of oil. The coexistence of oil and water lowers the mobility of the injected phase and raises the effective viscosity, and on the hydrophobic substrate the mixed fluids spread poorly, further increasing resistance. Progressive accumulation of scale particles and precipitates reduces the effective flow cross-section, so maintaining a nominally constant inflow requires a higher driving pressure, consistent with more severe scaling and pore-throat blockage in Chip 2.

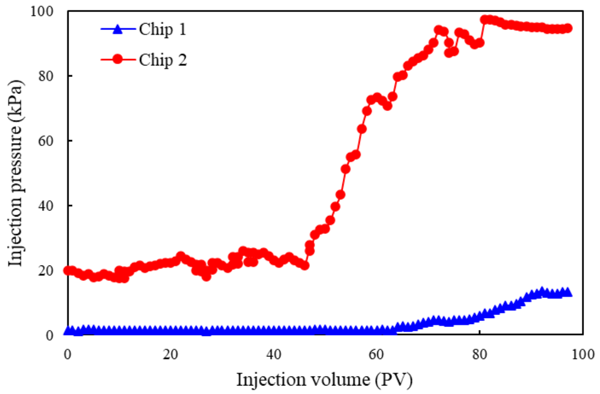

Figure 16: Injection pressure versus injected volume for oil-free Chip 1 and oil-bearing Chip 2. Oil presence increases baseline pressure and steepens the pressure-escalation segment.

Images from Chips 1 and 2 were binarized to quantify pore space retention over time. Pore space retention decreased monotonically with injection time, from 100% to 92% in Chip 1 and from 100% to 73% in Chip 2, the latter exhibiting a substantially larger loss (Fig. 17). The presence of kerosene promoted organic deposition and facilitated the nucleation and growth of inorganic scales. Deposits first occluded small pores and subsequently encroached on larger ones, leading to a marked reduction in overall pore space. Compared with the oil-free case, oil saturation led to larger and more continuous deposits (Fig. 15), which translated into a much steeper pressure buildup (Fig. 16) and a sharper loss of open pore space (Fig. 17). These three observations consistently indicate that oil-enhanced organic deposition provides nucleation/collection sites for inorganic scales, accelerating composite plugging.

3.4.2 Effect of Saturated Hydrocarbon Type on Scaling Behavior

Chips 3 and 4 showed broadly similar scaling dynamics, with negligible deposition at early injection and prominent dark deposits at late injection (Fig. 18). Spatial patterns and morphologies diverged. In the n-hexane case, Chip 3 developed blocky and band-like aggregates localized near the matrix walls, preferentially occluding small throats. In the n-tetradecane case, Chip 4 exhibited pervasive black accumulations across pore regions, with pronounced piling at the inlet, deposits adhered to walls and also formed agglomerates within flow channels, lodging in pore throats. These observations indicate that the heavier saturate promotes more widespread and severe blockage.

To quantify deposit size, scale particles in the microfluidic chips were measured. In Chip 3, lateral sizes ranged from 12 to 98 µm, whereas in Chip 4 they spanned 25 to 125 µm, indicating larger aggregates and more pronounced scaling under tetradecane. Mechanistically, a higher carbon number entails greater molecular weight and stronger van der Waals interactions; in addition, chain flexibility and intermolecular entanglement elevate the viscosity of long-chain n-alkanes [38,39]. Increased viscosity raises flow resistance and residence time, thereby facilitating nucleation and growth of deposits. Moreover, as carbon number increases, solubility decreases, making organic components more prone to precipitation and providing nuclei for subsequent aggregation. These factors jointly explain the larger deposits and stronger accumulation observed with tetradecane.

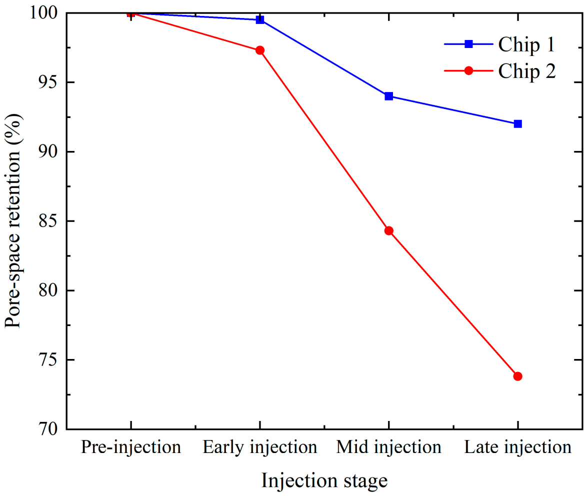

Figure 17: Pore space retention of different injection stages of Chip 1 and Chip 2.

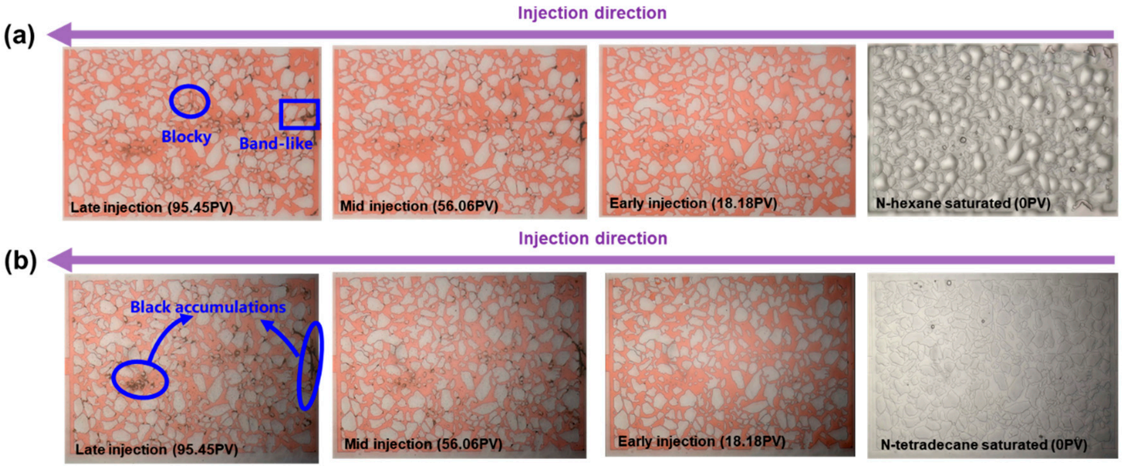

Figure 18: Scale formation during injection water injection process in Chip 3 and Chip 4. (**a**) Chip 3. (**b**) Chip 4.

As shown in Fig. 19, the injection pressure in Chip 4 rose from 21.97 kPa to 64.07 kPa, whereas Chip 3 increased from 13.32 kPa to 42.78 kPa. This contrast is attributed to the viscosity difference between the two n-alkanes at 50°C, with n-hexane ≈ 0.2 mPa·s and n-tetradecane ≈ 1.2 mPa·s. Linear fitting of the pressure-time records yielded slopes of 0.44 for Chip 3 and 0.67 for Chip 4, indicating a more pronounced rise in the presence of tetradecane. The higher oil viscosity increases viscous losses and prolongs residence time in preferential flow paths, which facilitates nucleation and growth of scale, diminishes effective pore space, and accelerates pore blockage, thereby steepening the pressure trajectory. By contrast, with the lower-viscosity saturated hydrocarbon, deposits remained sparse and dispersed as dot-like or patchy features along pore walls, and the associated pressure increase was correspondingly milder.

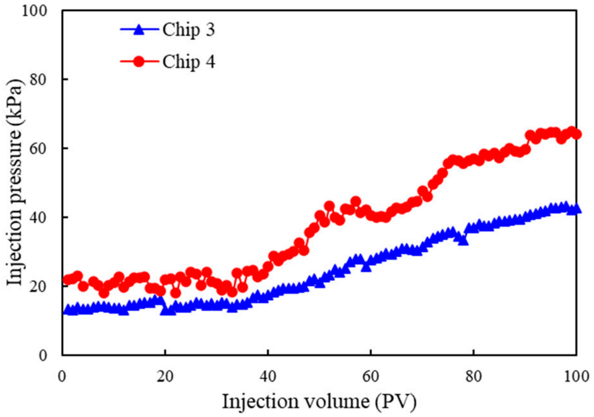

Figure 19: Injection pressure curves of Chip 3 and Chip 4.

The pore space retention curves for Chips 3 and 4 are shown in Fig. 20. Retention decreased monotonically with injection time in both cases, with the n-tetradecane chip exhibiting the largest loss, from 100% to 84.7%. Compared with n-hexane, the higher molecular weight and viscosity of n-tetradecane promoted water holdup and narrowed effective flow paths, which enhanced scale nucleation and accumulation and ultimately intensified pore blockage. By implication, reservoirs containing more complex, higher-molecular-weight saturated hydrocarbons are prone to more severe scaling and pore-throat plugging, higher injection pressures, and lower water-injection efficiency [40].

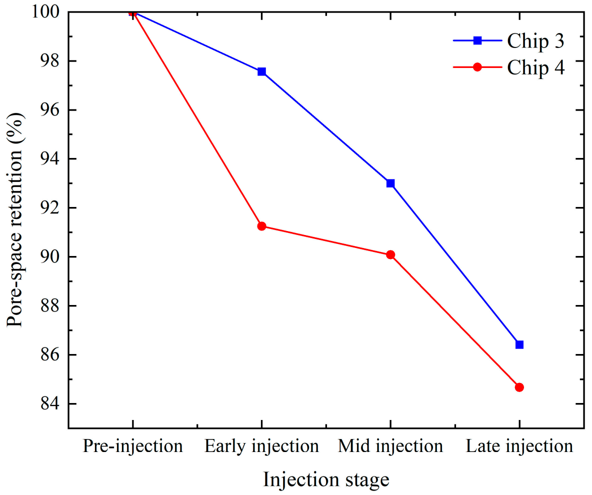

Figure 20: Pore space retention of different injection stages of Chip 3 and Chip 4.

3.4.3 *Effect of Wettability on Scaling Behavior*

Fig. 21 shows scaling Scale formation during injection water injection process in Chip 5 (hydrophilic glass) and Chip 6 (hydrophobic PDMS). In both chips, abundant scale was generated, appearing not only as wall-attached patches around the solid matrix but also as divergent growth emanating from localized nucleation sites into adjacent flow channels. Although Chip 5 exhibited more frequent scale formation events, its overall coverage by black deposits was lower than that of Chip 6. In Chip 5, deposits were predominantly blocky, with occasional slender band-like aggregations, and only minor accumulation was observed; most deposits appeared brown and were dispersed near the matrix. By contrast, in Chip 6 the deposits were largely black and piled up along matrix edges, forming more continuous accumulations that promoted pronounced pore- and throat-occlusion.

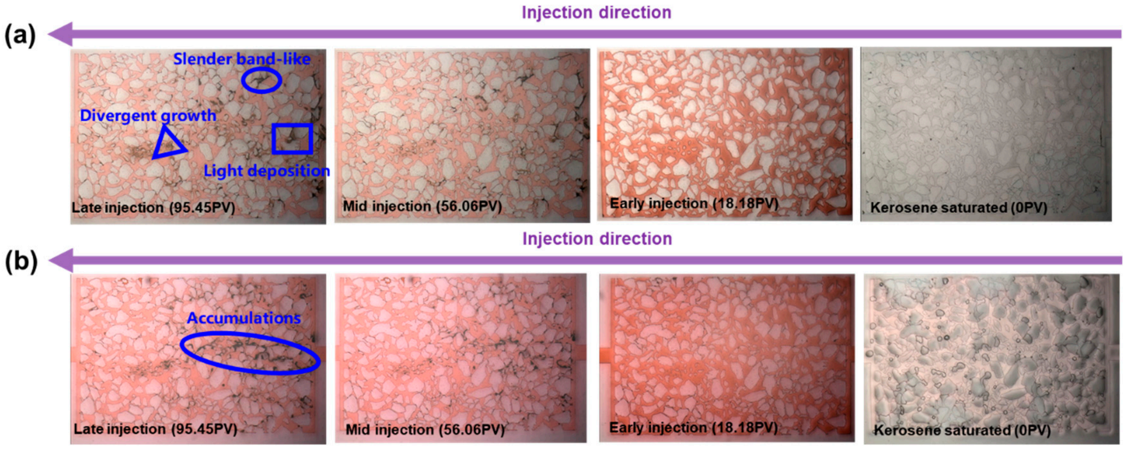

Figure 21: Scale formation during injection water injection process in Chip 5 and Chip 6. (**a**) Chip 5. (**b**) Chip 6.

Chip 6 exhibited markedly stronger deposit agglomeration than Chip 5. Size measurements on late-stage images show that the lateral extent of deposits in Chip 6 ranged from 29–437 µm, whereas Chip 5 yielded 18–192 µm, indicating more vigorous growth and clustering in Chip 6. Wettability governed the ease of water invasion and local residence time. In Chip 6, injected water spread poorly along pore walls and was prone to local entrapment within a complex, fine-scale network, which prolonged water–water contact and favored nucleation and growth of mineral scale, ultimately producing a larger deposit burden. By contrast, on hydrophilic surfaces the invading water coated the matrix more uniformly and flushed incipient crystallites more effectively, yielding smaller clusters and a higher fraction of open pore space. Moreover, during oil-saturated runs the hydrophobic matrix retained a thicker, more continuous oil film that narrowed the effective flow channels and enhanced capture of suspended particles and crystallites, whereas Chip 5 supported thinner, less persistent oil films that were more readily displaced by the injected water, resulting in weaker agglomeration.

Injection pressure curves of Chip 5 and Chip 6 is shown in Fig. 22. In Chip 5, pressure rose from 5.58 kPa to 8.24 kPa. In Chip 6, it increased from 20.4 kPa to 93.6 kPa. Linear regression of the growth segment yielded an apparent slope of 0.026 for Chip 5 and 2.09 for Chip 6, indicating a much steeper escalation on the hydrophobic surface and, by inference, more severe pore-channel constriction.

The divergence is consistent with wettability-controlled flow partitioning at the pore scale. On water-wet walls, injected water spreads as continuous films along pore boundaries and capillary forces assist displacement, promoting more uniform advance and partial flushing of incipient deposits. On oil-wet walls, water fails to wet the surface, capillary forces oppose advance, and oil films confine water into narrow rivulets; the effective cross-section and conductance are reduced, interfacial contact with resident brine is intensified, and supersaturation hot-spots favor nucleation and growth of mineral scale, often in synergy with organic fouling. The resulting aggregation at throats accelerates blockage and explains the sharp pressure build-up observed for Chip 6. These mechanisms align with established understandings of wettability effects on two-phase flow and waterflood efficiency [41–43].

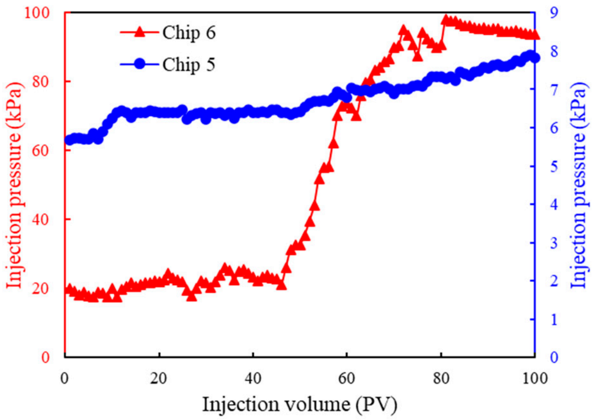

Figure 22: Injection pressure curves of Chip 5 and Chip 6.

Pore space retention of different injection stages of Chip 5 and Chip 6 is shown in Fig. 23. In the early stage, no visible scale had formed and both chips exhibited similar retention. With continued injection, retention declined monotonically. Chip 6 showed a pronounced drop from about 97% to 73%, whereas Chip 5 remained above 90%. The larger loss in Chip 6 is consistent with more confined aqueous pathways, higher local supersaturation, and a greater density of nucleation sites, which jointly favor scale nucleation and growth and accelerate throat occlusion [44]. The accompanying pressure rise and reduction in effective pore volume imply poorer sweep and diminished displacement efficiency, which translates into lower movable oil and reduced recovery in water-injection operations [45]. The hydrophobic substrate exhibited more persistent and aggregated deposits (Fig. 21), a markedly higher pressure growth rate (Fig. 22), and a lower pore space retention (Fig. 23), evidencing a wettability-controlled amplification of scaling and organic-inorganic co-deposition.

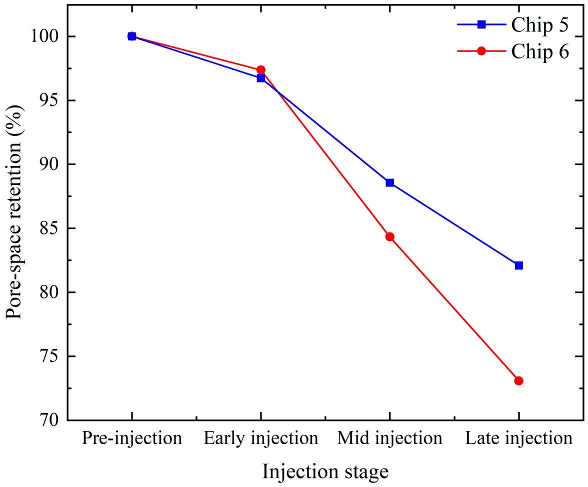

Figure 23: Pore space retention of different injection stages of Chip 5 and Chip 6.

3.4.4 Effect of Asphaltene Content on Scaling Behavior

Fig. 24 shows scaling Scale formation during injection water injection process in Chip 7 (2% VO-79) and Chip 8 (6% VO-79). Following injection of reinjected water, both microchips saturated with alkanes containing an asphaltene surrogate developed dark-brown to black deposits that increased in size and number with time. Pronounced accumulations formed near the inlet in both tests. As asphaltene concentration increased, deposit morphology evolved from sparse, isolated attachments along the matrix walls to extensive band-like agglomerations that occupied the flow channels. In Chip 7, deposits appeared mainly as dot-like and blocky features distributed around the substrate. In Chip 8, numerous banded aggregates formed, covering broader regions and occluding a large fraction of the pore space. Collectively, the observations indicate a strong positive association between asphaltene content and the severity of pore blockage.

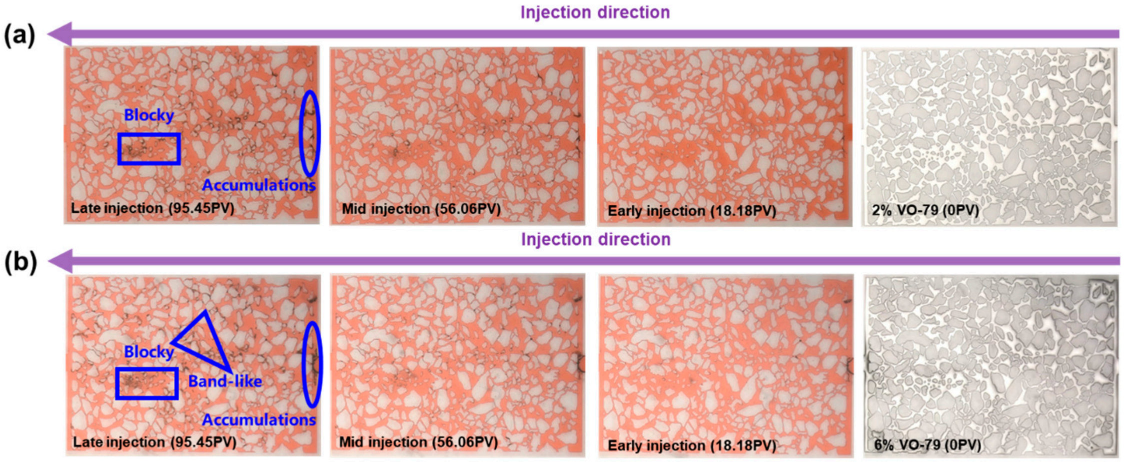

Figure 24: Scale formation during injection water injection process in Chip 7 and Chip 8. (**a**) Chip 7. (**b**) Chip 8.

As the content of asphaltene-like species increased, aggregation and pore-channel plugging became progressively more pronounced, with conspicuous deposit banks forming at the inlet. This behavior is consistent with a cooling-induced precipitation mechanism: when the heated model oil encountered colder injection water, the abrupt temperature drop lowered the solubility of asphaltene-type components, promoting rapid nucleation and growth [46]. The inlet region, where the fluids first contact and residence time is relatively high, favored accumulation and gradual stacking of precipitates, ultimately restricting flow [47].

In Chip 7, the lateral size of scale agglomerates ranged from 34–128 μm, whereas in Chip 8 it increased to 46–145 μm, indicating larger deposits at higher asphaltene-surrogate content. Two factors likely contribute. First, asphaltenes raise oil viscosity and strengthen intermolecular associations, which slows displacement and lengthens water–water contact, favoring supersaturation and crystal growth. This trend is widely reported for crude oils as asphaltene content increases [48]. Second, asphaltenes adsorb at the oil-water interface, lower interfacial tension and stabilize water-in-oil dispersions, thereby increasing interfacial area and mixing, which promotes nucleation and growth of inorganic scales when brines are incompatible [49]. The inorganic component of the deposits is consistent with oilfield observations that mixing of injection and formation waters drives carbonate/sulfate scaling in porous media [50].

Injection pressure increased monotonically as deposits accumulated (Fig. 25). In Chip 7 the pressure rose from 44.46 kPa to 64.40 kPa, and in Chip 8 from 59.09 kPa to 78.23 kPa, with Chip 8 exhibiting the highest overall values. This trend is consistent with the rheology and stability of asphaltene-rich oils, where greater asphaltene content increases bulk viscosity and aggregation propensity, thereby raising flow resistance during water injection [51]. Upon water injection, compositional and thermal perturbations destabilize asphaltene aggregates; lower temperature accelerates precipitation, leading to pore-scale deposition and permeability loss, which manifests as a sustained pressure rise in core and micromodel floods [52]. These mechanisms explain the larger pressure build-up and more severe plugging observed in the higher-asphaltene system of Chip 8.

The injection pressure curves of Chip 7 and Chip 8 exhibit a second, consistent trend. As the asphaltene-surrogate content increases, the initial quasi-steady period shortens and the pressure rises earlier. This behavior is attributable to the higher interfacial activity of asphaltenes, which lowers oil-water interfacial tension and accelerates emulsification and mixing, thereby reducing the induction time before deposition initiates [53]. When the injected and formation brines are geochemically incompatible, faster mixing promotes earlier nucleation and growth of mineral scales such as $CaCO_3$ or $BaSO_4$, leading to rapid pore occlusion and a steeper pressure increase [54]. The resulting co-presence of organic matter and inorganic scale is known to intensify formation damage by combining emulsion blockage with crystalline deposition, consistent with the pressure response observed at 6% VO-79 [55].

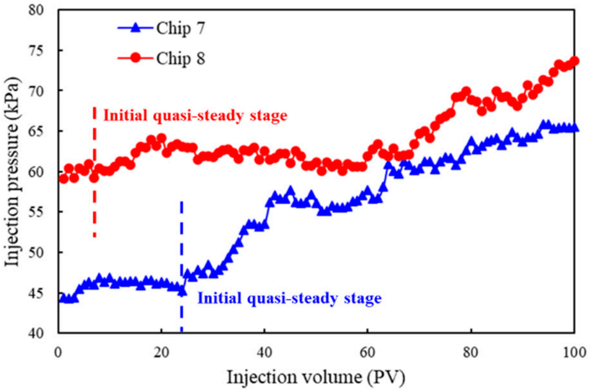

Figure 25: Injection pressure curves of Chip 7 and Chip 8.

Pore space retention of different injection stages of Chip 7 and Chip 8 is shown in Fig. 26. At the mid-injection stage, pore space retention in Chip 7 was 91.7%, lower than 93.9% in Chip 8, attributable to heterogeneous asphaltene-surrogate distribution that promoted inlet-side precipitation and early throat occlusion in Chip 7. By late injection stage, higher asphaltene content clearly accelerated occlusion. In Chip 8 the open pore fraction declined from 98.0% at the outset to 67.9%, indicating more extensive plugging. Mechanistically, increasing asphaltene content raises oil viscosity and enhances oil-water interfacial interactions, which favors organic precipitation and provides nucleation sites for mineral scale, yielding composite deposits and severe throat blockage, especially near the inlet. Similar near-wellbore impairment by asphaltene precipitation during injection has been widely reported [56], and pore-scale microfluidic studies corroborate rapid deposit formation and permeability loss under water invasion.

These observations align with established flow-assurance and formation-damage literature [57]. Asphaltene precipitation and deposition reduce injectivity, alter wettability, and promote coupled organic–inorganic fouling; microfluidic and modeling works further show that asphaltene-rich systems exhibit stronger aggregation and faster pore-scale plugging under waterflood-like conditions [58].

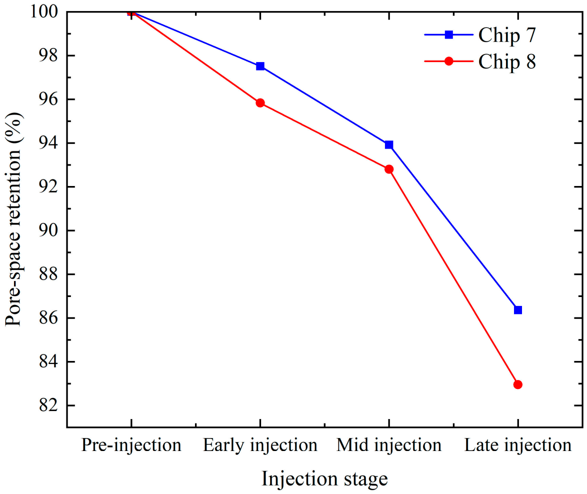

Figure 26: Pore space retention of different injection stages of Chip 7 and Chip 8.

4 Conclusion

This work clarifies the pore-scale mechanisms responsible for injectivity decline in the M tight oil reservoir by integrating long-duration core floods with NMR T_2 spectra, MICP, SEM EDS, and factor-controlled microfluidic visualization. The combined evidence shows that incompatibility between sulfate-rich injection water and formation water drives carbonate and sulfate scaling, while oil wet surfaces and oil-borne heavy fractions, notably asphaltenes, amplify organic and inorganic co-deposition. Damage is strongly size selective, medium and large pores are preferentially occluded, which leads to sustained pressure rise and permeability loss. The conclusions of this work can be summarized as follows:

(1) After 12–24 h of injection, core permeability fell by 61%–73%, evidencing contraction of effective flow paths. NMR shows small-pore porosity retention remained high, whereas medium/large pores suffered pronounced losses, confirming that larger conduits attract higher flux and accumulate more precipitates and fines.

(2) SEM reveals wall-attached granular deposits after injection, and EDS mapping identifies Ca and Ba signals co-located with C and Ca in pores, which is consistent with $CaCO_3$ and $BaSO_4$ infilling produced by mixing of incompatible brines under reservoir conditions.

(3) Microfluidics demonstrates substantially stronger deposition in oil-bearing runs, injection pressure increased from 20.4 to 93.6 kPa with oil and from 1.3 to 13.4 kPa without oil, pore space retention fell from 100% to 73% and from 100% to 92%, respectively. Oil films and emulsified droplets promote particle capture, extend residence time, and enable composite organic and inorganic plugging.

(4) Heavier saturated hydrocarbons intensified the blockage. With n-tetradecane, pressure rose from 21.97 to 64.07 kPa and pore space retention fell to 84.7%, which is worse than the result with n-hexane where pressure rose from 13.32 to 42.78 kPa. Higher viscosity narrows active channels, increases supersaturation, and accelerates nucleation and growth.

(5) On hydrophobic, that is, oil-wet, substrates, deposits became larger and more continuous with late injection stage lateral sizes of 29 to 437 μm compared with 18 to 192 μm for hydrophilic chips. The pressure escalation was much steeper, from 20.4 to 93.6 kPa compared with 5.58 to 8.24 kPa, and the loss of open pore area was greater, falling to about 73% compared with more than 90%. Water wet conditions helped distribute flow and partially flush incipient crystallites.

(6) Increasing the content of the asphaltene surrogate intensified bank formation near the inlet and caused early throat occlusion. In the higher asphaltene case, pore space retention declined from 98.0% to 67.9% and pressure increased from 59.09 to 78.23 kPa, indicating rapid development of composite organic and inorganic deposits and a shorter induction period before plugging.

This study primarily focuses on the microscopic mechanisms of scale formation in tight oil reservoirs. Upscaling of insights from microfluidic observations into near-wellbore models will be investigated in future studies.

Acknowledgement: Not applicable.

Funding Statement: This work is supported by the Science and Technology Project of PetroChina Company Limited (Grant No. 2023ZZ17YJ05).

Author Contributions: The authors confirm contribution to the paper as follows: study conception and design: Yong Wang, Qingqing Cao; data collection: Changhao Yan; analysis and interpretation of results: Xinyu Tang; draft manuscript preparation: Dingxue Zhang; review: Jingyi Zhu. All authors reviewed and approved the final version of the manuscript.

Availability of Data and Materials: The datasets generated and/or analyzed during the current study are available from the corresponding authors on reasonable request.

Ethics Approval: Not applicable.

Conflicts of Interest: The authors declare no conflicts of interest.

References

1. Malozyomov BV, Martyushev NV, Kukartsev VV, Tynchenko VS, Bukhtoyarov VV, Wu X, et al. Overview of methods for enhanced oil recovery from conventional and unconventional reservoirs. Energies. 2023;16(13):4907. [CrossRef].
2. Gong Z, Zhang L, Zhang T, Yan Z, Cong S, Zhou Z, et al. Evaluation of the compatibility between formation and injection water in ultra-low permeability reservoirs. Processes. 2024;12(11):2475. [CrossRef].
3. Moghadasi J, Jamialahmadi M, Müller-Steinhagen H, Sharif A. Formation damage due to scale formation in porous media resulting from water injection. In: Proceedings of the SPE International Symposium and Exhibition on Formation Damage Control; 2004 Feb 18–20; Lafayette, LA, USA. [CrossRef].
4. Merdhah ABB, Yassin AAM. Scale formation due to water injection in Berea sandstone cores. J Appl Sci. 2009;9(18):3298–307. [CrossRef].
5. Mehdizad A, Pourafshary P, Sedaee B. Visual investigation of simultaneous clay swelling and migration mechanisms and formation damage consequences using micromodels. J Petrol Sci Eng. 2022;214:110561. [CrossRef].
6. Mohammed I, Mahmoud M, El-Husseiny A, Al Shehri D, Al-Garadi K, Kamal MS, et al. Impact of asphaltene precipitation and deposition on wettability and permeability. ACS Omega. 2021;6(31):20091–102. [CrossRef].
7. Kordestany A, Hassanzadeh H, Abedi J. An experimental approach to investigating permeability reduction caused by solvent-induced asphaltene deposition in porous media. Can J Chem Eng. 2019;97(1):361–71. [CrossRef].
8. Lo PA, Tinni AO, Milad B. Experimental study on the influences of pressure and flow rates in the deposition of asphaltenes in a sandstone core sample. Fuel. 2022;310:122420. [CrossRef].
9. Ding B, Dong M, Chen Z, Kantzas A. Enhanced oil recovery by emulsion injection in heterogeneous heavy oil reservoirs: experiments, modeling and reservoir simulation. J Petrol Sci Eng. 2022;209:109882. [CrossRef].
10. Wang W, Wei W, Ferrier N, Arismendi N. Scale formation and inhibition study for water injection wells. In: Proceedings of the SPE International Oilfield Scale Conference and Exhibition; 2018 Jun 20–21; Aberdeen, UK. [CrossRef].

11. Tang Y, Mu T, Qin J, Peng R, Liu M, Xie Y. The mechanism of reservoir damage by water injection in ultra-low-permeability reservoirs and optimization of water quality index. Energies. 2025;18(6):1455. [CrossRef].
12. Bin Merdha AB, Mohd Yassi AA. Scale formation due to water injection in Malaysian sandstone cores. Am J Appl Sci. 2009;6(8):1531–8. [CrossRef].
13. Lin L, Xu C, Lyu H, Chen Y, Cong S, Yang X, et al. Property changes of low-permeability oil reservoirs under long-term water flooding. Processes. 2024;12(11):2317. [CrossRef].
14. Zhou Y, Yang W, Yin D. Experimental investigation on reservoir damage caused by clay minerals after water injection in low permeability sandstone reservoirs. J Pet Explor Prod Technol. 2022;12(4):915–24. [CrossRef].
15. Li J, Liu W, Cong S, Li Y, Zheng K, Luo X, et al. The flow of water-in-oil emulsion in heterogeneous parallel model. J Petrol Sci Eng. 2022;208:109209. [CrossRef].
16. Farajollahi S, Bazvand M, Tahernejad E. Asphaltene deposition effects on reservoir rock wettability and modification strategies. Heliyon. 2024;10(21):e38436. [CrossRef].
17. Okere CJ, Sheng JJ, Fan LK, Huang XW, Zheng LH, Wei PF. Experimental study on the degree and damage-control mechanisms of fuzzy-ball-induced damage in single and multi-layer commingled tight reservoirs. Petrol Sci. 2023;20(6):3598–609. [CrossRef].
18. Lu Y, Liu K, Wang Y. Applying NMR T_2 spectral parameters in pore structure evaluation—an example from an Eocene low-permeability sandstone reservoir. Appl Sci. 2021;11(17):8027. [CrossRef].
19. Harrison AL, Dipple GM, Song W, Power IM, Mayer KU, Beinlich A, et al. Changes in mineral reactivity driven by pore fluid mobility in partially wetted porous media. Chem Geol. 2017;463:1–11. [CrossRef].
20. Nikoo AH, Malayeri MR. Impact of hydrodynamic and interfacial interactions on scale formation in a capillary microchannel. Langmuir. 2021;37(46):13746–56. [CrossRef].
21. Lv Q, Zheng R, Zhou T, Guo X, Wang W, Li J, et al. Visualization study of CO_2-EOR in carbonate reservoirs using 2.5D heterogeneous micromodels for CCUS. Fuel. 2022;330:125533. [CrossRef].
22. Cai J, Yang J, Huang Z, Xu S, Zhang L, Wang H. Quantitative evaluation of residual acid invasion and flowback in fractured-vuggy carbonate reservoirs using microfluidics. Energies. 2025;18(5):1162. [CrossRef].
23. Zacherl L, Baumann T. Quantification of scalings in dynamic environments using a combination of Quartz Crystal Microbalance and Raman Microscopy. Adv Geosci. 2024;65:9–17. [CrossRef].
24. Neuman SP. Theoretical derivation of darcy's law. Acta Mech. 1977;25(3):153–70. [CrossRef].
25. Zhu J, Tang X, Li X, Wen Y, Deng Z, Rao D, et al. The reservoir injury rules of water injection to an ultralow permeability reservoir: experimental research based on core-NMR and microfluidic technology. Energy Fuels. 2024;38(16):15131–46. [CrossRef].
26. Wang Z, Zhang Y, Liao H. Experimental investigation on precipitation damage during water alternating flue gas injection. Oil Gas Sci Technol Rev IFP Energ Nouv. 2020;75:45. [CrossRef].
27. SY/T 6169-2021. Classification of oil reservoir. Beijing, China: China Standards Press; 2021. (In Chinese).
28. Wang HZ, Zhang L, Kang X, Kang WL, Li Z, Yang HB. Effect of CO_2 on physical properties of produced oil and water in Changqing and emulsion stabilization mechanism. China Surfactant Deterg Cosmet. 2023;53(6):617–24. (In Chinese).
29. Wang LS, Zhao XD, Liu WF, Xie ZR, Wu XY, Guo DF, et al. Microcosmic occurrence state of low saturation reservoir and origin of high content of resin and asphaltene in Maxi Slope, Junggar Basin. Chin J Geol. 2023;58(4):1325–39. (In Chinese). [CrossRef].
30. Wang ZX, Wang YL, Sun ZP, Zhu SZ, Wang H, Xu L, et al. Geochemical characteristics and oil-source correlation of bitumen in sandstone of Chang-8 member in southwestern Ordos Basin. Mar Orig Pet Geol. 2017;22(2):31–9. (In Chinese). [CrossRef].
31. Cui CZ, Yi JQ, Zong R, Li GQ, Zhao JM, Jiang MJ, et al. Change law of reservoir physical properties based on nuclear magnetic resonance technology. Sci Technol Eng. 2024;24(14):5790–6. (In Chinese).
32. Liu JS, Liu JB, Liu XH, Peng JF. Cause analysis of water injection well plugging in M oilfield and study on measures for plug removal and injection increase. Drill Prod Technol. 2021;44(1):129–32. (In Chinese).
33. Vetter OJ, Kandarpa V, Harouaka A. Prediction of scale problems due to injection of incompatible waters. J Petrol Technol. 1982;34(2):273–84. [CrossRef].

34. Kamal MS, Hussein I, Mahmoud M, Sultan AS, Saad MAS. Oilfield scale formation and chemical removal: a review. J Petrol Sci Eng. 2018;171:127–39. [CrossRef].
35. Wang Y, Li H, Zhu Y, Jiang J. Experimental study on formation damage caused by emulsified oil droplets during water injection. J Southwest Pet Inst. 2003;25(1):43–6. (In Chinese).
36. Tu Y, Wang WY, Wu M, Guan L, Yu M. Analysis of scaling influencing factor on water injection system in water-injected oilfield. Oil Gas Storage Transp. 2010;29(2):97–109. (In Chinese).
37. Vazirian MM, Charpentier TVJ, de Oliveira Penna M, Neville A. Surface inorganic scale formation in oil and gas industry: as adhesion and deposition processes. J Petrol Sci Eng. 2016;137:22–32. [CrossRef].
38. Riesco N, Vesovic V. Extended hard-sphere model for predicting the viscosity of long-chain n-alkanes. Fluid Phase Equilib. 2016;425:385–92. [CrossRef].
39. Liu HB, Guo XQ. Influence of property and structure of crude oil on its viscosity. Xinjiang Pet Geol. 2008;29(3):347–9. (In Chinese).
40. MacKay EJ, Jordan MM, Torabi F. Predicting brine mixing deep within the reservoir, and the impact on scale control in marginal and deepwater developments. In: Proceedings of the International Symposium and Exhibition on Formation Damage Control; 2002 Feb 20–21; Lafayette, LA, USA. [CrossRef].
41. Sedghi M, Gong Y, McCaskill B, Bai S, Wang R, Piri M, et al. Pore-to-core upscaling of two-phase flow in mixed-wet porous media: Part II-a dynamic pore-network modeling approach. Transp Porous Media. 2024;151(13):2561–600. [CrossRef].
42. Goryntseva KY, Markova R, Kemalov AF. Methods of fighting against scale build-up at the Tuymazy deposit. Int J Appl Eng Res. 2015;10(24):45360–5.
43. Agbalaka C, Dandekar AY, Patil SL, Khataniar S, Hemsath JR. The effect of wettability on oil recovery: a review. In: Proceedings of the SPE Asia Pacific Oil and Gas Conference and Exhibition; 2008 Oct 20–22; Perth, Australia. [CrossRef].
44. Tzachristas A, Kanellopoulou DG, Koutsoukos PG, Paraskeva CA, Sygouni V. The effect of surface wettability on calcium carbonate precipitation in packed beds. Surf Interfaces. 2022;34:102354. [CrossRef].
45. Luo W, Kottsova A, Vardon PJ, Dieudonné AC, Brehme M. Mechanisms causing injectivity decline and enhancement in geothermal projects. Renew Sustain Energy Rev. 2023;185:113623. [CrossRef].
46. Maqbool T, Srikiratiwong P, Fogler HS. Effect of temperature on the precipitation kinetics of asphaltenes. Energy Fuels. 2011;25(2):694–700. [CrossRef].
47. Al-Hosani A, Ravichandran S, Daraboina N. Review of asphaltene deposition modeling in oil and gas production. Energy Fuels. 2021;35(2):965–86. [CrossRef].
48. Olajire AA. A review of oilfield scale management technology for oil and gas production. J Petrol Sci Eng. 2015;135:723–37. [CrossRef].
49. Zhang S, Zhang L, Lu X, Shi C, Tang T, Wang X, et al. Adsorption kinetics of asphaltenes at oil/water interface: effects of concentration and temperature. Fuel. 2018;212:387–94. [CrossRef].
50. Belkacem O, Rezrazi A, Aizi K, Abdelouahed L, Laidi M, Touil A, et al. Prediction of barite scale formation and inhibition in hydrocarbon reservoirs using AI modeling: focus on different optimization algorithms. Results Eng. 2025;26:105222. [CrossRef].
51. Ghanavati M, Shojaei MJ, SA AR. Effects of asphaltene content and temperature on viscosity of Iranian heavy crude oil: experimental and modeling study. Energy Fuels. 2013;27(12):7217–32. [CrossRef].
52. Li M, Tian Y, Wang C, Jiang C, Yang C, Zhang L. Effect of temperature on asphaltene precipitation in crude oils from Xinjiang oilfield. ACS Omega. 2022;7(41):36244–53. [CrossRef].
53. Peng Y, Zhang X, Cheng L, Zhang H, Tang J, Chen H, et al. Effect of asphaltenes on the stability of water in crude oil emulsions. Materials. 2025;18(3):630. [CrossRef].
54. BinMerdhah AB, Yassin AAM, Muherei MA. Laboratory and prediction of barium sulfate scaling at high-barium formation water. J Petrol Sci Eng. 2010;70(1–2):79–88. [CrossRef].
55. Saraji S, Goual L, Piri M. Adsorption of asphaltenes in porous media under flow conditions. Energy Fuels. 2010;24(11):6009–17. [CrossRef].
56. Nasrabadi H, Moortgat J, Firoozabadi A. New three-phase multicomponent compositional model for asphaltene precipitation during CO_2 injection using CPA-EOS. Energy Fuels. 2016;30(4):3306–19. [CrossRef].

57. Mahdavifar M, Roozshenas AA, Miri R. Microfluidic experiments and numerical modeling of pore-scale asphaltene deposition: insights and predictive capabilities. Energy. 2023;283:129210. [CrossRef].
58. Mozaffari S, Ghasemi H, Tchoukov P, Czarnecki J, Nazemifard N. Lab-on-a-chip systems in asphaltene characterization: a review of recent advances. Energy Fuels. 2021;35(11):9080–101. [CrossRef].